Multiple-frequency tomography of the upper mantle beneath the African/Iberian collision zone

Mickaël Bonnin,[1] Guust Nolet,[1] Antonio Villaseñor,[2] Josep Gallart[2] and Christine Thomas[3]

[1]*Géoazur, université de Nice/Sophia-Antipolis, CNRS, observatoire de la Côte d'Azur,* 250 *rue A. Einstein, F-06560 Valbonne, France.*
E-mail: mbonnin@geoazur.unice.fr
[2]*Institute of Earth Sciences 'Jaume Almera', CSIC, Carrer de Lluís Solé i Sabaris, E-08028 Barcelona, Spain*
[3]*Westfälische Wilhelms Universität, Institut für Geophysik, Corrensstraβe 24, D-48149 Münster, Germany*

SUMMARY

During the Cenozoic, the geodynamics of the western Mediterranean domain has been characterized by a complex history of subduction of Mesozoic oceanic lithosphere. The final stage of these processes is proposed to have led to the development of the Calabria and Gibraltar arcs, whose formation is still under debate. In this study, we take advantage of the dense broad-band station networks now available in the Alborán Sea region, to develop a high-resolution 3-D tomographic *P* velocity model of the upper mantle beneath the African/Iberian collision zone that will better constrain the past dynamics of this zone. The model is based on 13200 teleseismic arrival times recorded between 2008 and 2012 at 279 stations for which cross-correlation delays are measured with a new technique in different frequency bands centred between 0.03 and 1.0 Hz, and for the first time interpreted using multiple frequency tomography. Our model shows, beneath the Alborán Sea, a strong (4 per cent) fast vertically dipping anomaly observed to at least 650 km depth. The arched shape of this anomaly, and its extent at depth, are coherent with a lithospheric slab, thus favouring the hypothesis of a westward consumption of the Ligurian ocean slab by roll-back during Cenozoic. In addition to this fast anomaly in the deep upper mantle, high intensity slow anomalies are widespread in the lithosphere and asthenosphere beneath Morocco and southern Spain. These anomalies are correlated at the surface with the position of the Rif and Atlas orogens and with Cenozoic volcanic fields. We thus confirm the presence, beneath Morocco, of an anomalous (hot?) upper mantle, but without clear indication for a lateral spreading of the Canary plume to the east.

Key words: Seismic tomography; Subduction zone processes; Continental tectonics: compressional; Dynamics of lithosphere and mantle; Africa; Europe.

1 INTRODUCTION

Western Mediterranean evolution, through the last 30 Myr, is usually acknowledged to be related to the southward rollback of the Mesozoic Alpine Tethys and Ligurian ocean slabs, causing the progressive opening of the Cenozoic Liguro-Provençal and Tyrrhenian basins between southern France and Italy, of the Algerian basin between the Balearic Islands and Algeria and finally of the Alborán Sea basin between Spain and Morocco (e.g. Jolivet *et al.* 2006). The opening of these basins then lead to the accretion of Peloritan/Calabrian, Kabilies and Alborán continental terranes on the Apulian, north African and Iberian margins, respectively. Though this scenario is relatively robust for the easternmost western Mediterranean—from tomographic studies, present day volcanism and seismicity (Faccenna *et al.* 2004)—the

geodynamic evolution of the southern and western domains remains unclear.

Difficulties mostly crystallize in the geodynamic processes that led to the structure and geometry of the Alborán Sea and Gibraltar arc. Questions remain, in particular, on the causes for the complex geological history of the Alborán continental domain, that is episodes of hot thermal metamorphism, uplift and thinning (Platt & Whitehouse 1999), respectively. To address this problems, many efforts have been made since the 90s trying to image the upper mantle structure beneath western Mediterranean. Studies based on body waves seismic tomography (Blanco & Spakman 1993; Spakman *et al.* 1993; Seber *et al.* 1996a; Mezcua & Rueda 1997; Morales *et al.* 1999; Bijwaard & Spakman 2000; Wortel & Spakman 2000; Piromallo & Morelli 2003; Spakman & Wortel 2004), systematically evidenced the presence, beneath the Gibraltar region, of a fast
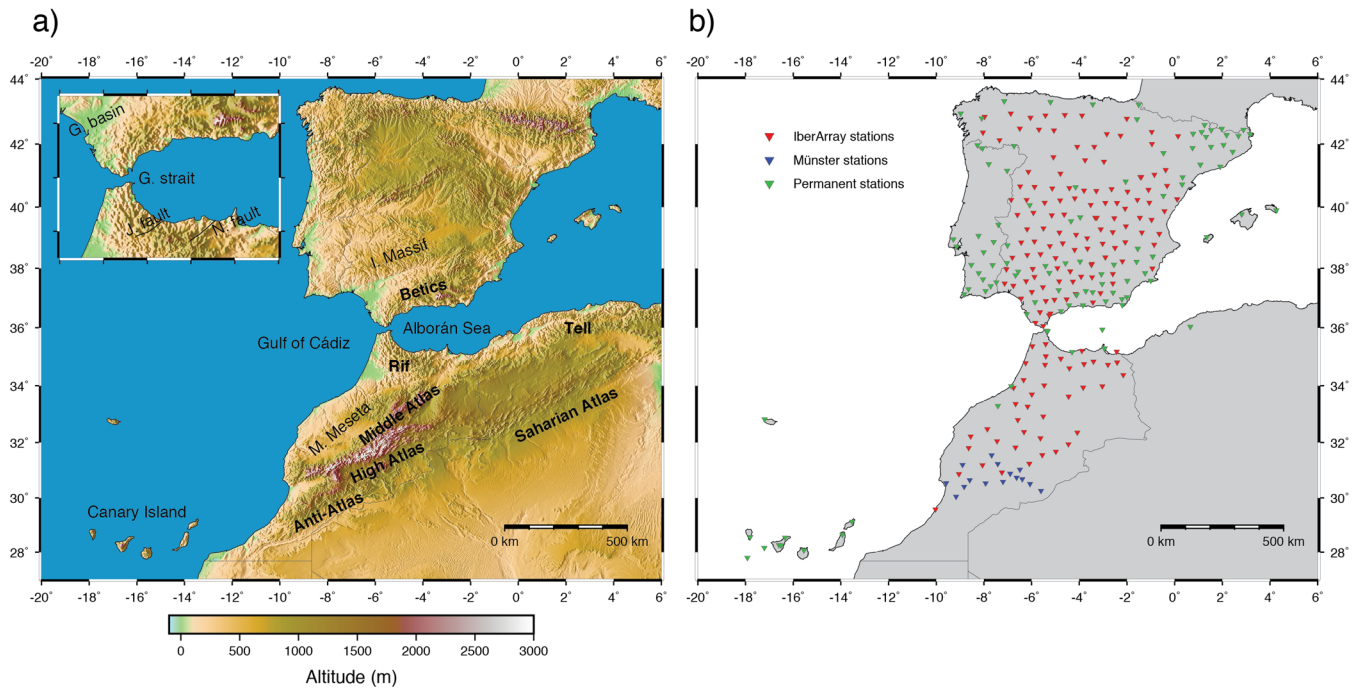
Figure 1. (a) Topography map of the Alborán Sea region with the cited localities. M. Mesata, Moroccan Meseta; I. Massif, Iberian Massif; G. basin, Guadalquivir basin; G. strait, Gibraltar strait; J. fault, Jehba fault; N. fault, Nekor fault. (b) Location of the stations used for this study. Colours define the different networks: green, permanent stations; red, IberArray stations; blue, Morocco-Münster stations.

velocity anomaly at ∼ 100 to ∼ 700 km depth. However, due to the sparsity of the receiver coverage at that time, only blurred and large-scale pictures of the mantle were obtained, causing the publication of a variety of models to interpret these images. They can roughly be separated into three sets: (i) a delamination of the lithospheric mantle of the Alborán lithosphere (Seber *et al.* 1996a; Calvert *et al.* 2000), (ii) a removal of the thickened continental lithosphere that would have resulted from collision between Africa and Iberia (Platt & Vissers 1989; Platt & Houseman 2003) and (iii) sinking of a lithospheric slab resulting from consumption of the Ligurian ocean during slab roll-back (Blanco & Spakman 1993; Spakman *et al.* 1993; Gutscher *et al.* 2002, 2012). Recent studies based on other seismological approaches such as *SKS* splitting analysis (Buontempo *et al.* 2008; Díaz *et al.* 2010) or dispersion of *P*-waves (Bokelmann & Maufroy 2007) or on the existence of deep seismicity (Buforn *et al.* 2011) tend to favour the third model, though a consensus has not emerged. To finally settle the debate, two major seismic experiments were designed to generate high-resolution pictures of the upper mantle beneath this region: the Program to Investigate Convective Alborán Sea System Overturn (PICASSO) and the IberArray deployment. Recently, this data set has been analyzed by Bezada *et al.* (2013) using a simplified finite-frequency approach for detecting *P*-waves velocity anomalies.

Another open key question we want to address in this region concerns the origin of the massive Cenozoic volcanic activity observed throughout Morocco (Lustrino & Wilson 2007). It is proposed to be linked with the Atlas ranges asymmetry (Teixell *et al.* 2005; Missenard *et al.* 2006; Duggen *et al.* 2009, and references therein), that is the higher topography observed in the western (High, Middle and Anti) Atlas compared with eastern (east High and Saharan) Atlas (see Fig. 1a for location) while they faced close to the same amount of convergence (Frizon de Lamotte *et al.* 2000).

Seber *et al.* (1996b)—based on seismologic stations located throughout Morocco—previously imaged slow *P*-wave anomalies in the uppermost mantle (50 to 350 km depth) beneath Moroccan Atlas, thus evidencing the presence in this region of an anomalous (hot?) mantle. Several models are proposed that invoke: (i) delamination of the High and Middle Atlas (see Fig. 1a for location) lithospheric mantle as a consequence of lithospheric thickening caused by the Africa/Iberia convergence (Ramdani 1998); (ii) a plume related anomaly (Missenard *et al.* 2006); (iii) a combination of plume and subduction return flow (Duggen *et al.* 2004, 2005, 2009; Frizon de Lamotte *et al.* 2009). One of the question posed by models (ii) and (iii) is the origin of the possible plume. An attractive solution would be a lateral connection of the Atlas domain with the Canary Island plume imaged by Montelli *et al.* (2004, 2006). The hot mantle could have risen from a deep superplume (Zeyen *et al.* 2005; Missenard *et al.* 2006) or could have been guided by the thinned Atlas lithosphere (Duggen *et al.* 2005, 2009; Frizon de Lamotte *et al.* 2009)—thinning inherited from early Mesozoic rifting episodes (e.g. Frizon de Lamotte *et al.* 2011).

To address those different key questions in relation with more large-scale western Mediterranean geodynamics, we take advantage of the dense networks now available in Iberia and Morocco to perform the first multiple-frequency teleseismic *P*-wave tomography (Sigloch *et al.* 2008) beneath the Africa/Iberia plate boundary. Thanks to the high density and high quality of the permanent and temporary broad-band networks available and to the gain in resolution made available by the multiple-frequency approach, we are able to better constraint the evolution of the upper mantle structure beneath Alborán Sea and Moroccan domains. We notably propose high-resolution images of the geometry of the fast anomaly previously observed beneath the Alborán Sea and new inferences for a highly anomalous lithosphere beneath most of Morocco.
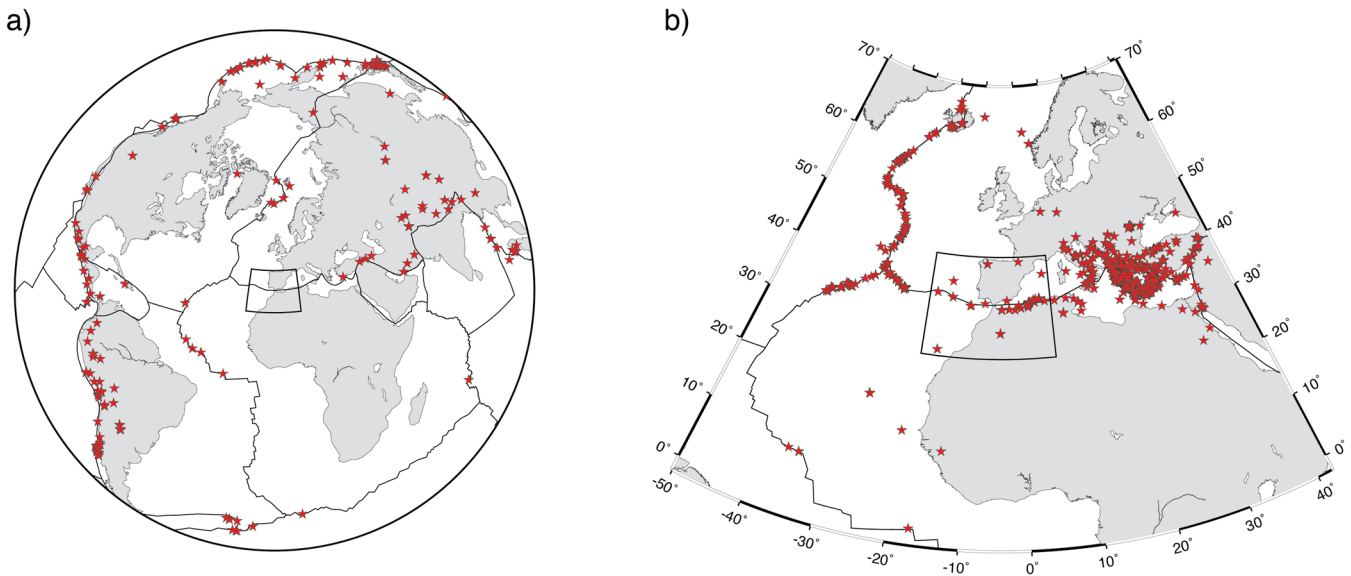
a)

b)

Figure 2. (a) Location of the 182 teleseismic events used in this study. (b) Location of the 633 local *P*-waves from the ISC catalogue. The boxes show the studied area.

2 TOMOGRAPHY STUDY

2.1 Data selection and methodology

2.1.1 Data

We use a set of 279 broad-band receiver stations from three networks. 106 stations from the Algerian, Moroccan, Portuguese and Spanish permanent networks; 159 temporary stations from the IberArray experiment and 15 temporary stations from the Morocco-Münster experiment (see Fig. 1b). For this network, we select teleseismic events with magnitude $M_w > 6$ in an epicentral distance range between 30° and 100° and we find 392 teleseismic events fitting our criteria. We deconvolve the seismograms from the receiver response to obtain the actual displacement and compute the theoretical arrival times using IASP91 Earth reference model (Kennett & Engdahl 1991). Crustal corrections are applied to take into account the variation in Moho depths using a local Moho depth model obtained from receiver function analysis on the same network (Mancilla *et al.* 2012, 2013a). For island stations (Canaries, Balearic) not honored by CRUST2.0 model (http://igppweb.ucsd. edu/~gabi/rem.html) the crustal corrections were determined from the station elevation using a *P*-velocity of 6.7 km s^{-1}. Events are then manually checked to remove bad quality signals from the database, reducing the number of teleseismic events to 182 (see Fig. 2a). This teleseismic data set is composed of ~13 200 source/station paths. Determination of the delay times is then performed using a modified version of the multichannel cross-correlation technique from VanDecar & Crosson (1990) in six frequency bands (centre frequencies of 0.03, 0.06, 0.13, 0.25, 0.5 and 1 Hz; see Section 2.1.2, and Appendices A and B for details on the approach). To perform relevant delay time measurements, we compute the cross-correlation only for frequency bands for which the amplitude in the broad-band spectrum of the stacked traces is higher than 20 per cent of the maximum amplitude.

To overcome the poor vertical resolution offered by teleseismic waves in the lithospheric part of the model, we add delay times of local *P* and *Pn* events from the International Seismological Center (ISC hereafter) catalogue. We select events between 1980 and 2008,

with $M_w > 5$, for epicentral distances ranging between 0° and 30° using ISC stations in Iberia and neighbouring countries. We obtain a total of 633 *P*-waves and 511 *Pn*-waves fitting our criteria, leading to approximately 23 700 and 16 000 source/station paths, respectively. Epicentres of the selected *P* and *Pn* events can be seen on Fig. 2(b).

2.1.2 Method

Cross-correlation delays are the preferred body wave observables in global tomography (e.g. Bolton & Masters 2001). For the estimation of global traveltime delays, either on broad-band signals or in different frequency bands, Sigloch & Nolet (2006) developed a method for the estimation of body wave delays using a matched filter. The matched filter is a synthetic signal that requires the separate estimation of the source time function. An accurate method for estimating differential times of seismic arrivals without the need of a matched signal was developed by VanDecar & Crosson (1990), but so far it has been applied only to cross-correlation of seismograms over regional arrays. Houser *et al.* (2007) observed that waveforms can globally be sorted into clusters of similar waveforms, which suggests that it should be possible to measure differential times over large distances. Here, we present a modification of the VanDecar-Crosson method for global use, or at least over clusters that are extended geographically.

The waveform of a body wave arrival, and thus the cross-correlation between two stations, is influenced by a number of factors: crustal reverberations, source propagation effects, attenuation, supercritical reflections or triplications and the effects of diffraction and scattering due to heterogeneities inside the Earth. The effects of attenuation can often be corrected for and, if we choose our seismograms in suitable distance ranges, we can minimize the effect of triplications and supercritical reflections. Crustal effects beyond a simple delay can possibly be corrected for, though such corrections are still the subject of intensive research (Obayashi *et al.* 2004; Ritsema *et al.* 2009). We eliminate rupture propagation effects by selecting only events of modest size. That leaves the heterogeneity as the major factor to influence delay times found by cross-correlation. The arrival time itself is affected by
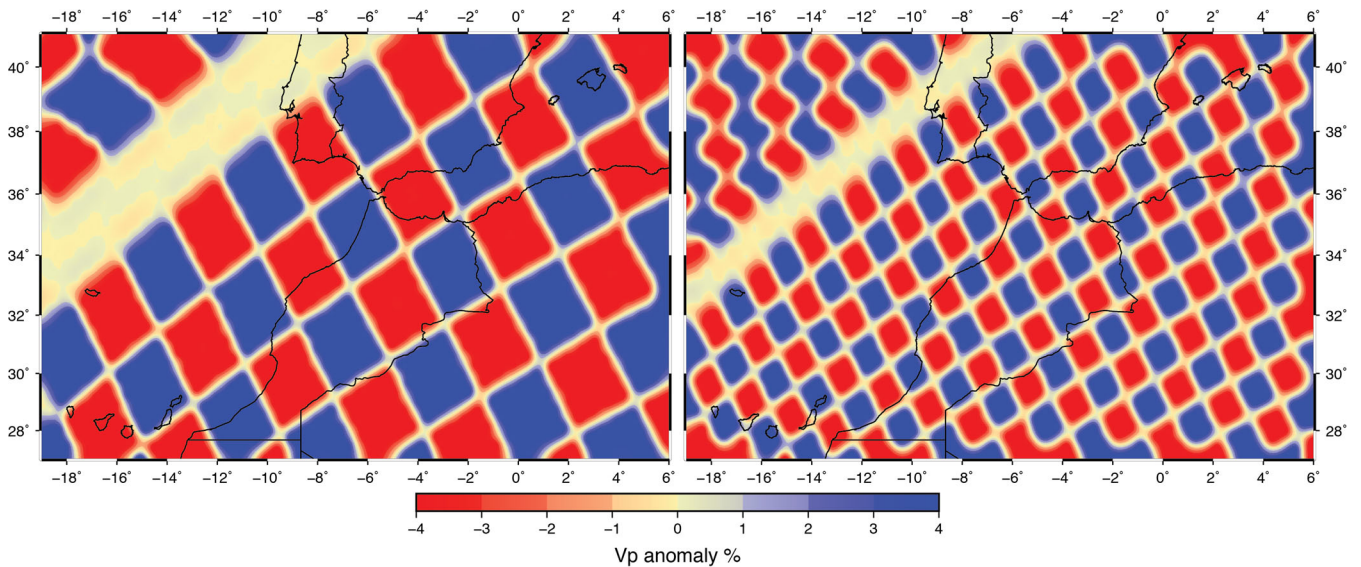
Figure 3. Horizontal cross-sections at 135 km depth through the input of (left) 300 km and (right) 150 km checkerboard tests.

large-scale differences in seismic velocity encountered along the way, whereas the waveform may be changed by smaller scale anomalies, thus introducing dispersion. Multiple frequency tomography (Sigloch *et al.* 2008) takes both the undispersed delay as well as the frequency-dependent delay caused by waveform changes into account, and assumes a linearized relationship between the amplitude of velocity anomalies and the observed cross-correlation delay. Mercerat & Nolet (2013) show that cross-correlation delays are indeed linear for the range of velocity contrasts found in the mantle.

For the formulation of the linear inverse problem we computed finite-frequency kernels using the theory of Dahlen *et al.* (2000) and numerical algorithms described in detail by Tian *et al.* (2007a,b) and Nolet (2008). The total number of data was 53 550. Using errors estimated as described in Appendix A, the final model fits the data with a relative χ^2 of 2. Though both studies used a combination of damping and smoothing, there are several important differences with the approach of Bezada *et al.* (2013)—who recently proposed a tomographic model based on close to the same data set. Even though both studies use a finite-frequency approach, kernels used by Bezada *et al.* (2013) are approximations, and for the traveltime outside of the Iberian region Bezada *et al.* (2013) assumed the background model to be correct, whereas we allowed for the whole Earth to influence the observed delays to avoid that heterogeneity or velocity bias elsewhere would map into the tomographic solution. Bezada *et al.* (2013) used only three high-frequency bands (0.3, 0.5 and 1 Hz), whereas we included both low frequencies (0.03 Hz) and the equivalent of infinite frequency (ISC delays, correctly interpreted with ray theory). The horizontal voxel size in both inversions is comparable: 42–56 km in Bezada's study, against 59–83 km in the cubed Earth parametrization used by us, and vertical spacing in the mantle is 35–55 against 44–90 km in our parametrization.

A major issue in tomographic studies is to estimate the way errors in the data propagate into the solution and the bias introduced by the regularization into the obtained solution. For large tomographic problems, the bias can be studied by generating a synthetic data set d_{synt}, adding an error distribution equal to that estimated for the real data for a known model m_{synt}, solving the system $Am = d_{synt}$, and comparing the solution m with m_{synt}.

2.2 Resolution tests

Here, we propose checkerboard tests for cell sizes of $2 \times 2 \times 2$ and $4 \times 4 \times 4$ voxels with alternate velocity anomalies of ±4 per cent (see Fig. 3). For ~300-km-wide cells, recovery of the geometry of the cells is excellent to good for the entire upper mantle, with the best results in the upper 250 km of the model (Fig. 4). Intensities of the anomalies (±4 per cent as input), are perfectly recovered at 70 and 135 km depth beneath Iberia, Morocco and Canary Island—thanks to the dense coverage offered by local *P* and *Pn* phases. At other depths, however, amplitudes are generally well recovered beneath Iberia but attenuated beneath Morocco (except at ~500 km depth). Attenuation of the amplitudes of the anomalies is close to 50 per cent in the major part of the model.

For ~150-km-wide cells (Fig. 5), recovery is very good for both geometry and shape for Iberia and Morocco between 30 and 250 km depth. At greater depths, recovery remains reliable for Iberia between 250 and 350 km depth but drops dramatically at deeper levels. Some shape recovering appears at ~500 km beneath Iberia but at the price of a poor recovery of the amplitudes (<25 per cent of the initial amplitudes).

2.3 Model description

Following the results from the resolution tests we will describe our model from the surface to 700 km depth for large-scale anomalies, but discuss small-scale features only in the top 300 km. We separate the description in two parts, guided by the nature and repartition of the main anomalies present in our model: the upper 200 km, where strong slow *P*-wave anomalies can be observed beneath Morocco and Southern Iberia; and the 150 to 700 km depth range, where a massive fast *P*-wave anomaly exists beneath Alborán Sea, Rif and Betics.

2.3.1 *Uppermost mantle low-velocity zones*

In the upper 200 km of our model (first top five panels in Fig. 6), the most striking features are the strong (>4 per cent from 10 to 70 km—>2 per cent at 135 km) slow anomalies observed: (i) at the shallowest depths, mostly beneath Rif, Betics and Gulf of Cádiz;
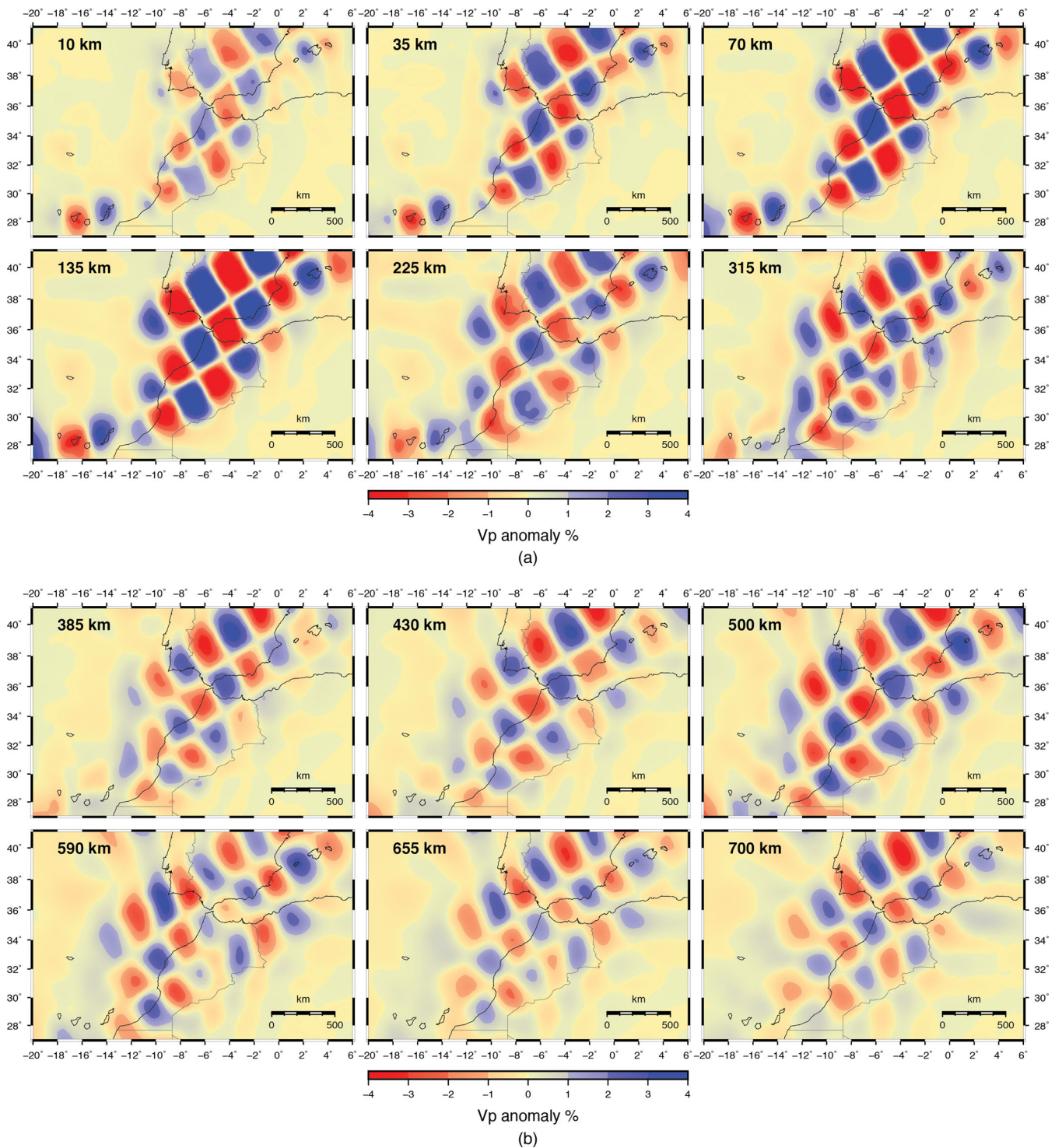
Figure 4. Horizontal cross-sections through the 300 km output checkerboard test.

(ii) at greater depths, beneath Moroccan Atlas, southern Spain, northeastern Morocco and Canary Islands.

    This bayonet shaped set of relatively continuous anomalies globally seems to circumvent high-velocity zones observed in the region mostly beneath western Morocco, Alborán Sea, southeastern and southwestern Iberia. Except for Alborán Sea that is composed by thinned continental lithosphere, those fast anomalies can be explained by the presence of old stable hercynian basements

(Moroccan Meseta and Iberian Massif). The fast anomaly associated with the Moroccan Meseta is particularly clear on Fig. 7, for cross-section AA′ (note that resolution tests for the vertical cross-sections are available as supplementary materials). In the top 50 km of the model, the strongest slow anomalies lie beneath the external domains of the Rif and Betics ranges and, to a lesser extent, beneath central High Atlas. At 70 km depth, the main anomaly—previously localized beneath Rif ranges—are found more to the west into the
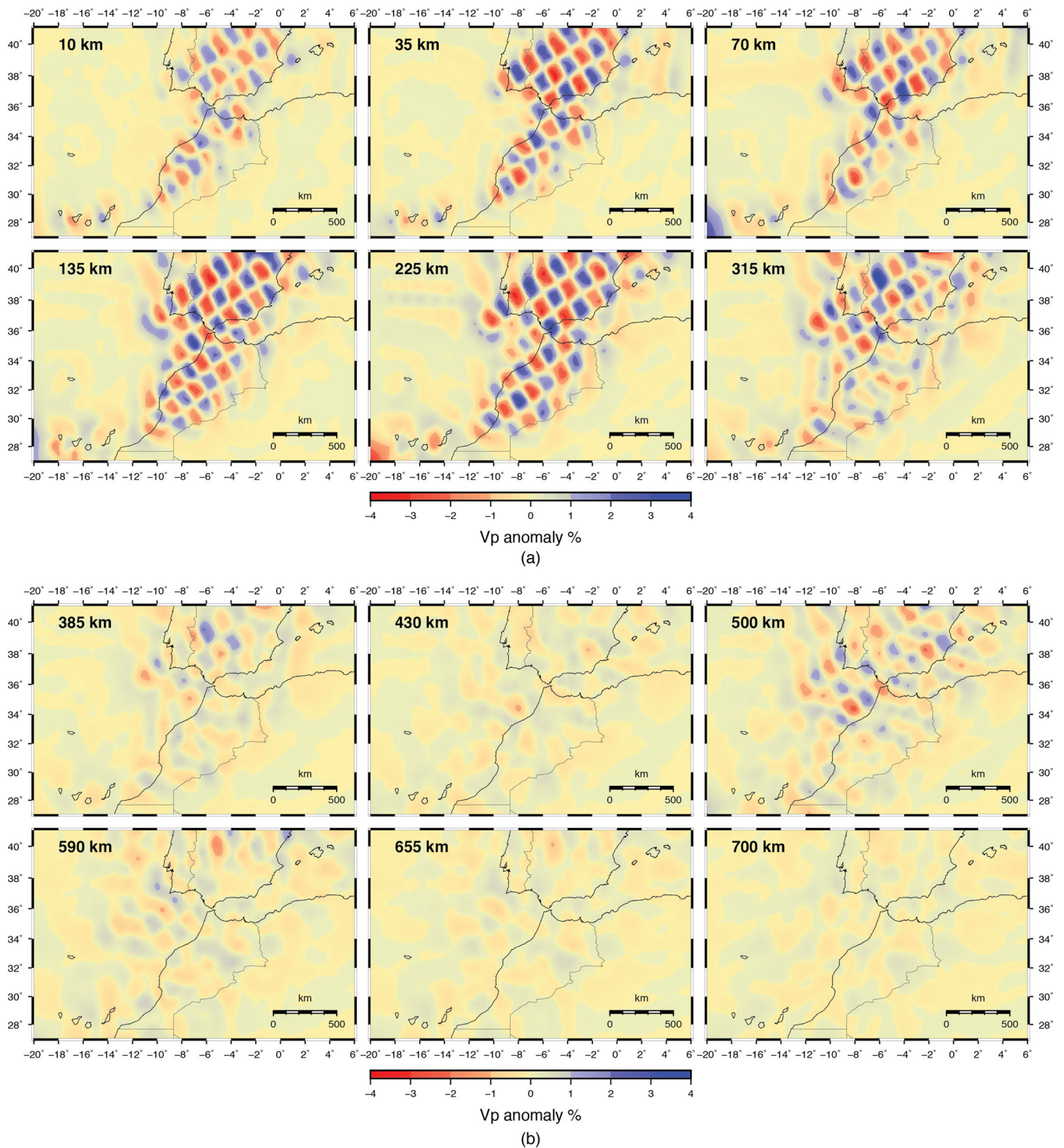
Figure 5. Horizontal cross-sections through the 150 km output checkerboard test.

gulf of Cádiz, while anomalies southeast of Iberia, in central Morocco and below the Canary Islands tend to increase in amplitude and in size.

At lower lithospheric depths (135 km on Fig. 6), one observes a continuous low-velocity zone from the Atlantic margin west of the High/Middle Atlas to the western Betics passing by the gulf of Cádiz (Fig. 7). The NNW/SSE oriented branch—that connects the High Atlas with the Betics (cross-section AA′)—is found even more to the west, skirting the strong fast anomaly lying in the eastern Rif

domain. The westward shift of this branch with depth is particularly clear along the vertical cross-sections CC′, DD′ and EE′ presented on Fig. 8 and evidences its relation with the position of the fast anomalies observed at deeper levels. Interestingly, this large-scale low-velocity zone correlates at the surface with the SW/NE oriented intraplate-type Cenozoic volcanic line (Missenard *et al.* 2006; Lustrino & Wilson 2007) whose main fields are shown by the open triangles on Fig. 6. Volcanic activity associated with Canary and Madeira archipelagos is also evident at those depths. Deeper than
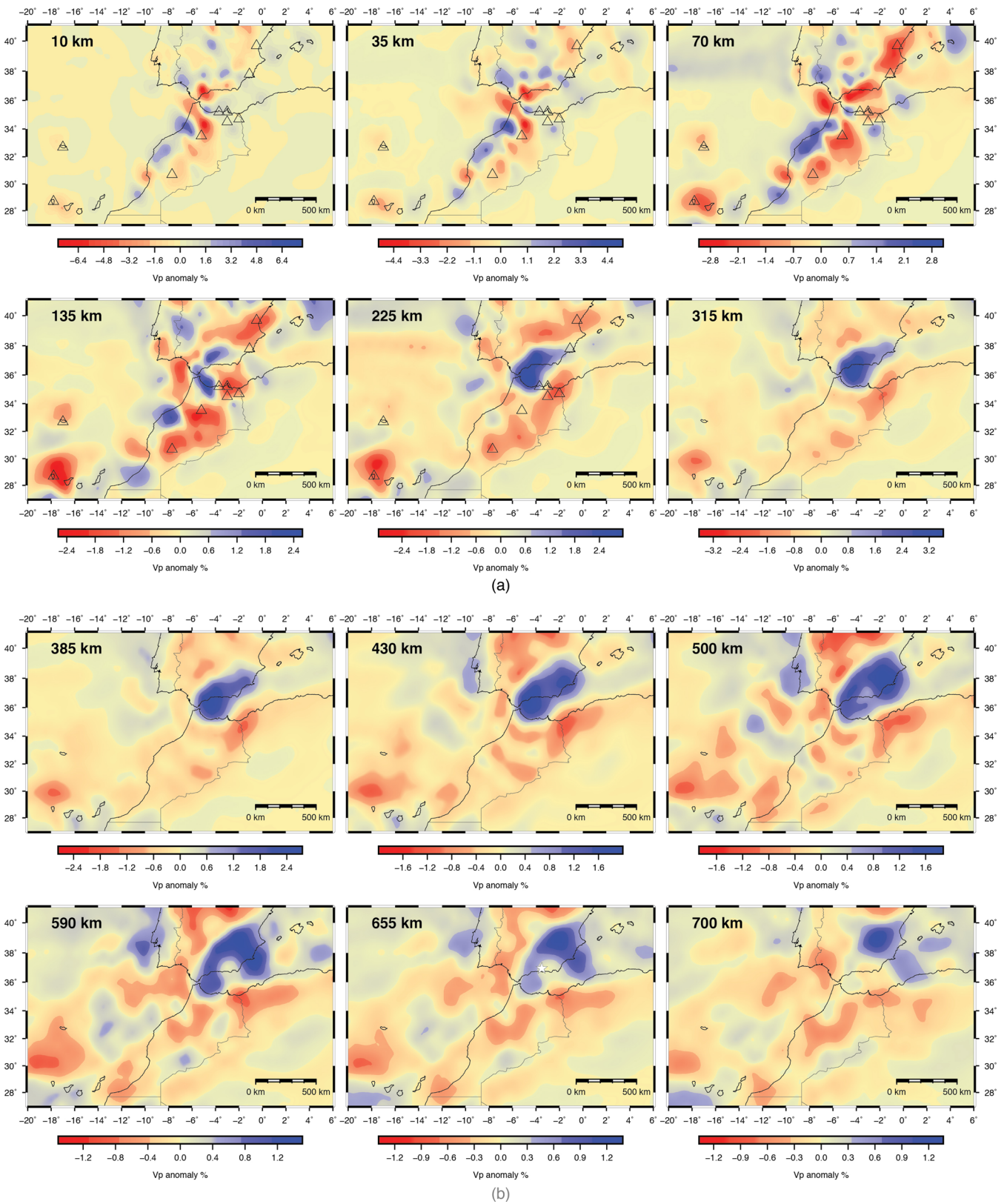
Figure 6. Horizontal cross-sections through the model between 11 and 700 km depth. Note that the colour-scale changes as a function of depth. Black triangles indicate the position of the main anorogenic Cenozoic volcanic fields (from Missenard *et al.* 2006; Lustrino & Wilson 2007). The white star on the 655 km depth cross-section is the projection at that surface of the focus (623 km) of the deep 2010 Granada earthquake.
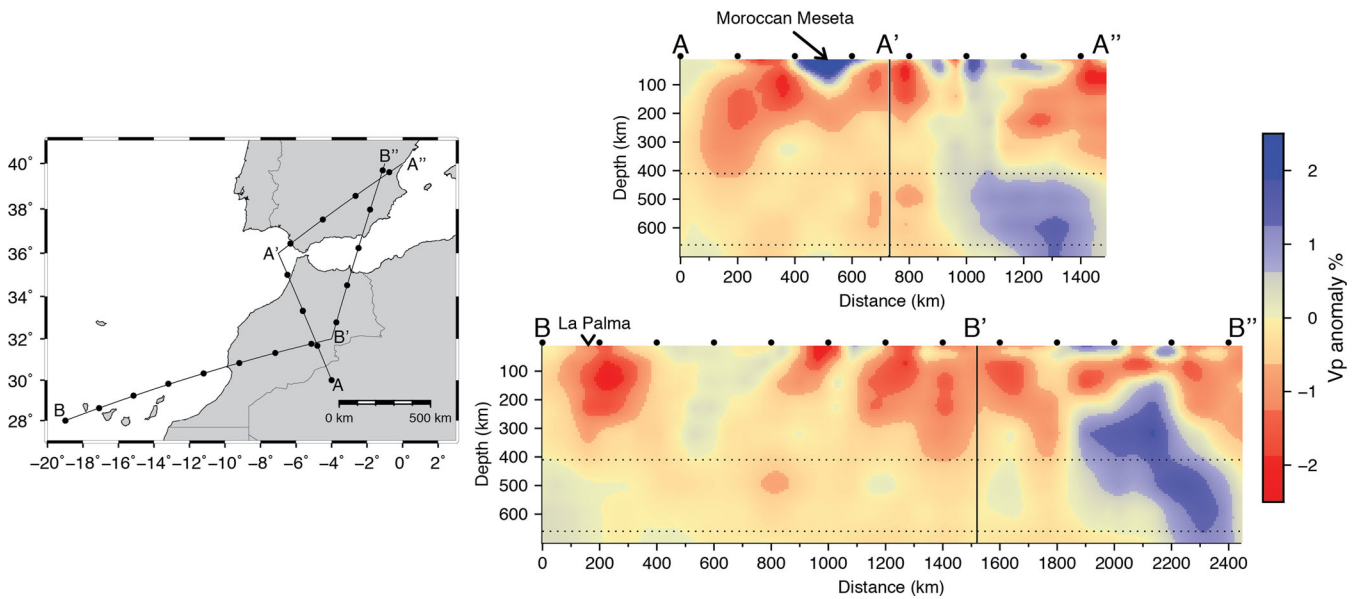
Figure 7. Vertical cross-sections focusing on the main slow anomalies observed in the top 300 km of the model. Section lines are indicated on the map, at left. Figs S1a and S1b provide resolution tests for the cross-section presented in this figure. Thick dotted black lines show limits of the transition zone.
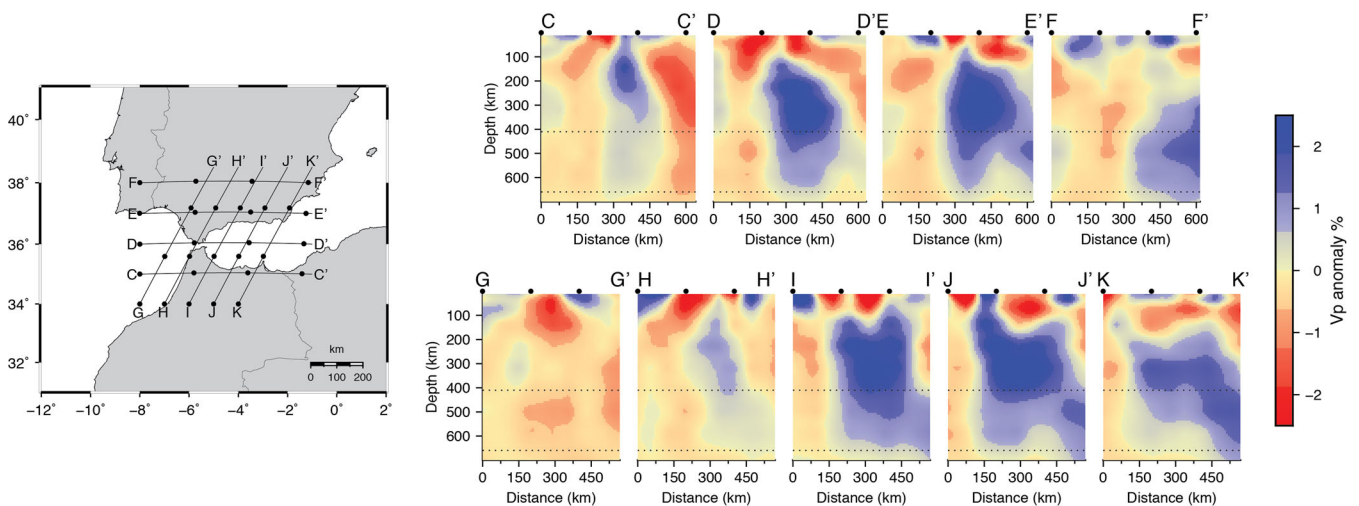

Figure 8. Vertical cross-sections focusing on the fast anomaly observed beneath the Alborán Sea. Section lines are indicated on the map, at left. Figs S2a and S2b provide resolution tests for the cross-sections presented in this figure. Thick dotted black lines show the limits of the transition zone.

200 km, the amplitude of the anomalies tends to decrease (except beneath the Canary Islands) but their geometry remains coherent with that at the shallowest levels.

The overall longitudinal trend of the low-velocity zone present beneath most parts of Morocco is shown by cross-sections AA″ and BB″, on Fig. 7. These slices show the clear continuity of the anomaly beneath most part of Morocco from the surface to approximately 300 km, vertically, and from the Atlantic coast to the Alborán Sea, horizontally in the east, and to the Guadalquivir basin passing by the gulf of Cádiz in the west. On both cross-sections these slow anomalies abruptly end in the vicinity of a high-velocity zone localized around the Alborán Sea basin. Beneath southern Spain, the low-velocity zone even seems to correlate with the overall shape of the fast anomalies (see northern part of BB″, NN′, PP′ and QQ′ cross-sections on Figs 7 and 9), likely indicating a link between these structures. Finally, Fig. 7 suggests that the strongest anomalies associated with the Canary Islands hotspot

are confined to the upper mantle, without continuation at greater depths.

2.3.2 Deep upper mantle fast anomalies

As slow anomalies tend to decrease in amplitude after 150 km depth, two—almost continuous—strong fast anomalies appear beneath the internal Rif and the western Betics. At about 200 km depth, anomalies combine to form a continuous high-velocity zone whose larger amplitudes (>2) per cent localize in a SW/NE narrow band (100 km wide, 250 km long) from the westernmost Alborán Sea to the central Betics (see horizontal cross-section at 225 km on Fig. 6). Lower amplitudes (1 to 2 per cent) form an arcuate anomaly—with concavity on the Alborán Sea side—extending from the Rif to the Betics and crossing the Alborán Sea. Its size, shape and localization remain relatively constant down to depths of ~400 km, suggesting that this
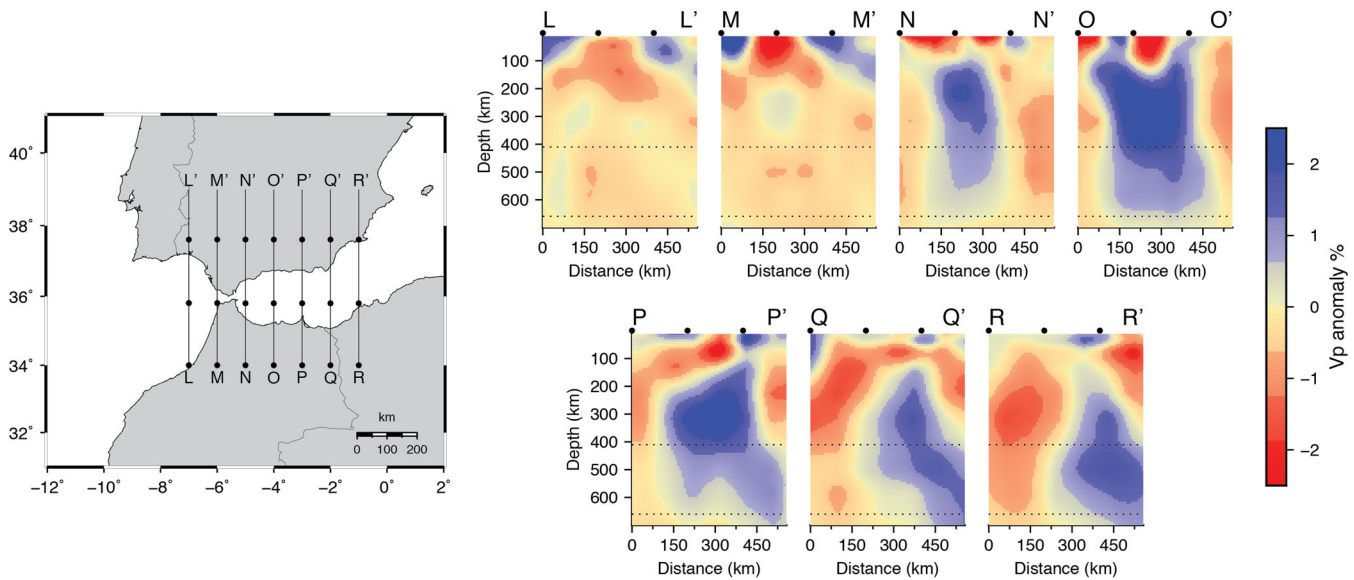
Figure 9. Vertical cross-sections focusing on the fast anomaly observed beneath Alborán Sea. Section lines are indicated on the map, at left. Figs S3(a) and S3(b) provide resolution tests for the cross-sections presented in this figure. Thick dotted black lines show the limits of the transition zone.

huge high-velocity zone stands close to vertical. When reaching the transition zone (410–660 km), the anomaly spreads out, accentuating its arcuate shape and developing a lobe, right beneath the south-easternmost part of Iberia. This lobe then tends to grow to the south, forming a second peak of intensity that can be observed down to 650 km.

Figs 8 and 9 present a set of vertical slices through the model focusing on the Alborán Sea domain in order to show the geometry of the high-velocity anomaly. The southernmost EW cross-section (CC′, Fig. 8) shows a high-velocity zone extending vertically from the surface to at least 300 km, likely down to 600 km. This anomaly is connected at the surface with the easternmost part of the Rif [in the tectonic unit delimited by Jehba and Nekor faults (Vergés & Fernàndez 2012)] and represents the southern edge of the high-velocity anomaly. Further to the north (cross-section DD′), crossing the strait of Gibraltar, the anomaly is still present at about 4°W in the middle of the Alborán Sea, and can be observed from 135 km down to 700 km depth. Note the absence of a connection with the surface. Therefore, our model does not show evidence for a continuous slab dipping towards the west from the gulf of Cádiz to the transition zone. Instead, the upper mantle beneath the Gulf of Cádiz is characterized by anomalously slow *P*-wave velocities (see Section 2.3.1). The Supporting Information Figs S4–S7 present additional resolution tests, checking the resolvability of the slow anomaly observed west the Gibraltar strait. They show that, while some smearing does exist, this structure is well resolved in the upper part of the model. The fast anomaly, that was relatively thin to the south (<100 km) increases in size to reach ∼ 200 km width with a gentle dip towards the east. Northward, along cross-section EE′, highest intensities are still observed around 4°W, between 150 and 700 km depth. Beneath the western Betics, this fast anomaly extends to depths shallower than 100 km suggesting some connection with the surface. Finally, high intensity fast anomalies disappear in the upper mantle along the last EW cross-section (FF′). The fast anomaly (attenuated compared with previous pictures) can be observed in the transition zone down to 700 km depth. This northeastern edge of the anomaly corresponds to the deep eastern lobe observed at great depths (500 to 700 km) in Fig. 6.

NS and NE/SW cross-sections on Figs 8 and 9 complete the description of the high-velocity anomaly. First of all, cross-sections GG′ (Fig. 8), LL′ and MM′ (Fig. 9) show, complementary to cross-section DD′, that no fast anomaly exist west the Gibraltar strait, beneath the gulf of Cádiz (see Supporting Information Figs S4–S7). Fast anomalies observed in the northern and southern borders of slices LL′ and MM′ are related to old stable hercynian basements such as the Moroccan Meseta and Iberian Massifs. The fast anomaly appears beneath the Betics (slice HH′) and the Alborán Sea (slice NN′) at about 5°W of longitude. The anomaly is about 150 km thick, lies in between 150 and 200 km down to 700 km (no connection with surface), and presents a slight dipping towards the north. Further east, the anomaly becomes massive (250 km thick), and covers the entire volume beneath the Alborán Sea. A connection with the surface seems present at around 6°W beneath the eastern Rif, at the intersection beneath lines CC′ and JJ′ and beneath the Betics as observed along line OO′. The anomaly still gently dips northward. Even further east, (cross-sections PP′ and QQ′) the anomaly is still located beneath a large part of the Alborán Sea (PP′) but tends to propagate northward beneath the southern coast of Spain (QQ′). The connection with the surface seems lost, except beneath the eastern Betics (PP′), and the space beneath the fast surface anomaly and the deepest one is filled by a low-velocity anomaly. The easternmost cross-sections (KK′ and RR′) show no connection with the surface, with the highest intensities localized between 300 and 500 km.

3 DISCUSSION

3.1 Lithospheric slow anomalies beneath Moroccan Atlas and Gibraltar arc

The strong low-velocity zones we image beneath most part of Morocco (Fig. 6) are a new piece of evidence for the presence of a strongly perturbed upper mantle beneath this area. The seismic station coverage now available in Morocco, as well as finite frequency approach, helped us resolving in great details the slow anomalies previously inferred in the uppermost mantle of Morocco (Seber *et al.* 1996b).

As detailed in the previous section, the southernmost part of the anomaly lies beneath the High, Middle and Anti Atlas ranges, laterally extending from the Moroccan Atlantic coast to the west, to approximately 3°W of longitude to the east. The extent of this anomaly correlates perfectly with the highest topographies of the Atlas ranges (see Fig. 1), these are proposed to be supported by density anomalies in the mantle, as they cannot be explained by the modest tectonics shortening estimated in this area (Teixell *et al.* 2003; Gomez *et al.* 1998). Lithospheric thinning is proposed (Zeyen *et al.* 2005; Missenard *et al.* 2006; Babault *et al.* 2008; Frizon de Lamotte *et al.* 2009) to account for the dynamic topography (Teixell *et al.* 2003, 2005), the Cenozoic volcanism (Lustrino & Wilson 2007; Duggen *et al.* 2009), the high thermal flow (Ramdani 1998) and the positive geoid anomalies (e.g. Missenard *et al.* 2006; Fullea *et al.* 2010) observed in the Moroccan Atlas domain. Our tomograms (Fig. 6) support this hypothesis by showing low-velocity anomalies whose size and amplitudes are maximal at 50 to 150 km depths and that correlate at the surface with the main Moroccan Cenozoic volcanic fields. In northern Morocco this correlation is, however, visible at greater depths (in between 130 to 300 km depth), likely indicating that lithospheric thinning ends south of this area. We note, in this region, a lack of low *P*-wave velocities in the uppermost part of our model probably indicating that connection between magma sources and the surface occurs along structures not thick enough (dikes?) to be resolved.

In a set of geodynamic models (Zeyen *et al.* 2005; Missenard *et al.* 2006; Frizon de Lamotte *et al.* 2009), the lithosphere thinning observed beneath Morocco is associated with a plume-like anomaly extending far northward and causing the Cenozoic intraplate volcanism described in western Mediterranean (Lustrino & Wilson 2007). Some models (Hoernle *et al.* 1995; Goes *et al.* 1999; Piromallo *et al.* 2008) even propose a connection between the Canary plume and the western European volcanism (French Massif Central, Eifel hotspot). Our study shows that such a SW/NE trending anomaly is not observed. Instead, the low-velocity zones skirt the fast anomalies detected in the upper mantle, forming a bayonet shaped slow perturbation around the Gibraltar arc (Fig. 6). This slow anomaly is not correlated at the surface with any known volcanic field or uncompensated crust but can, however, be the cause for the intense anatectic episodes observed in the internal Rif and Betics, dated at ~20 Ma (Cuevas *et al.* 2006; Rossetti *et al.* 2010, 2013).

Origins for the uncompensated Moroccan Atlas crust and for the Cenozoic volcanism is still a matter of debate; several models are proposed: (1) asthenospheric flow associated with roll-back of the Tethys slab (Teixell *et al.* 2005). (2) Delamination of the Atlas lithospheric mantle as a consequence of lithospheric overthickening with (Duggen *et al.* 2009) or (3) without Canary plume material flow (Ramdani 1998). (4) A large-scale mantle plume with deep reservoir extending from the Canaries to the western Mediterranean (Hoernle *et al.* 1995; Goes *et al.* 1999; Zeyen *et al.* 2005; Fullea *et al.* 2010). (5) Edge-driven convection due to a difference in lithosphere-asthenosphere boundary depth between the west African craton and Moroccan lithosphere (King & Ritsema 2000; Missenard & Cadoux 2012). Our tomograms cannot really favour one of these models but lead us to discard the second and fourth ones. Even if the resolution of our images dramatically drops east of the Canary archipelago, Fig. 7 tends to refute the hypothesis of a connection between Canary mantle plume and the Moroccan hot line (e.g. Duggen *et al.* 2009). Neither do slow anomalies seem to extend deeper than 300 km, thus apparently discarding the possibility for a deep mantle anomaly from which a small-scale plume could rise. At those depths, however, a relatively thin (<150 km) rising plume would probably not be resolved.

The origin of slow anomalies beneath Gibraltar arc (Rif, Gibraltar strait and Betics) is more speculative. Recently, Alpert *et al.* (2013) searched for the best combination of mantle flow and slab geometry beneath the Alborán domain to fit *SKS* fast polarization directions from Díaz *et al.* (2010) and Miller *et al.* (2013). They show that those *SKS* data are well explained by a southwestward mantle flow around a vertically dipping arcuate fast anomaly, presenting the shape observed in our model. To illustrate this, we plot, on Fig. 10, the averaged *SKS* splitting measurements used in their study (Díaz *et al.* 2010; Miller *et al.* 2013) on an horizontal cross-section of our model at 135 km depth. The fast directions of polarization are close to parallel to the general trend of the slow anomalies and indeed seem to skirt the high *P*-wave velocity zones beneath the Alborán Sea. We propose that this correlation between the *SKS* pattern and the trend of the low-velocity zones is due to the interaction between a horizontal mantle flow and some asthenospheric upwellings in the vicinity of slab tearing (see NN′, PP′ and QQ′ sections, on Fig. 9). During its rising, the asthenospheric material drifts around the high-velocity zones entrained by the southwestward mantle flow
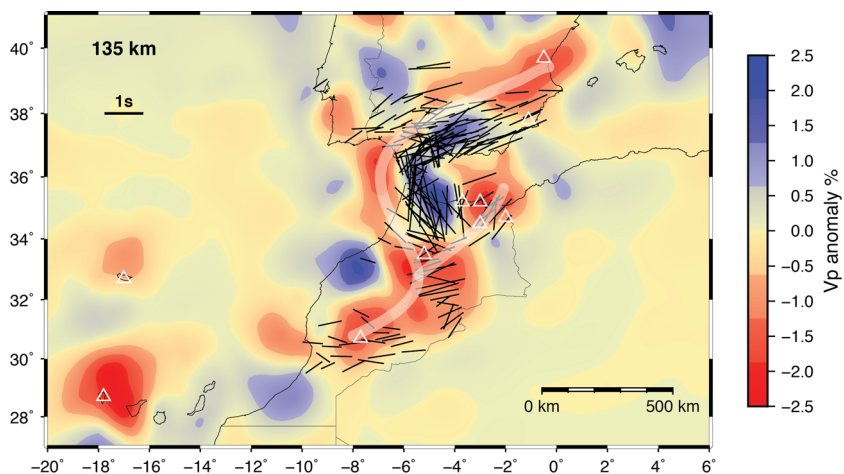
Figure 10. Horizontal slice at 135 km depth together with *SKS* splitting measurements from Díaz *et al.* (2010) and Miller *et al.* (2013). Strong slow anomalies observed beneath the central Morocco and the Gulf of Cádiz are associated with past (Morocco) and present (Canary Islands) volcanic activity (indicated by white triangles). Shaded line—parallel to the *SKS* splitting measurements—is the proposed mantle flow beneath the region.

proposed by Alpert *et al.* (2013). This can interestingly be compared to larger scale patterns in western Mediterranean and western Europe. Indeed, the intraplate volcanism in these regions is correlated with the presence, at depth (between 100 and 400 km depth), of slow *P*-wave anomalies that also skirt the remnants of subducted lithosphere along the Alpine collision belt (Piromallo *et al.* 2008), probably in response to the dynamics of the Tethyan subduction history.

3.2 Fast anomalies beneath Alborán Sea

The major issue to understand geodynamics at the African/Iberian plate boundary concerns the geological and tectonic history of the Alborán continental domain. In the last 30 Myr, this domain underwent low pressure high temperature metamorphism, uplift and overthrusting onto Iberian and African margins to form Betics and Rif orogens (Platt *et al.* 1998; Platt & Whitehouse 1999). These successive episodes are proposed to result either from lithospheric thickening followed by lithospheric detachment (e.g. Platt & Vissers 1989), delamination of the lithospheric mantle of the Alborán domain (e.g. Seber *et al.* 1996a; Calvert *et al.* 2000), rollback of a Tethyan oceanic slab (e.g. Blanco & Spakman 1993; Spakman *et al.* 1993; Gutscher *et al.* 2002), slab break off (Zeck 1996) or hybrid models proposing slab roll-back and lithosphere delamination (e.g. Duggen *et al.* 2004; Vergés & Fernàndez 2012).

The high-velocity zone we image beneath the western Mediterranean is consistent with a vertically dipping lithospheric slab. Its arcuate shape, vertical extent (down to 700 km depth) and localization—mostly beneath western Alborán and Betics—is not in agreement with detachment of an overthickened lithosphere (Platt & Vissers 1989) for which we would have expected a more blob-shaped anomaly. In this sense, we agree with Bezada *et al.* (2013) who show fast anomalies with close to the same geometry beneath Alborán Sea. In our opinion, based on the different vertical cross-sections discussed above (Figs 8 and 9), this anomaly is, however, not dipping eastward and there is no evidence for an active subduction process west of the Gibraltar Strait, as previously proposed (Bijwaard & Spakman 2000; Calvert *et al.* 2000; Gutscher *et al.* 2002, 2012). The vertical extent of the anomaly is also unlikely to result from lithospheric delamination alone (Seber *et al.* 1996a; Calvert *et al.* 2000), that would have represented a much smaller amount of material. Our preference thus goes to a model involving subduction process, associated with roll-back, the only known process to be able to generate such high-velocity zones in the upper mantle and to generate the deep seismicity observed beneath the Granada region (Buforn *et al.* 2011) (see white star on the 655 km depth panel on the Fig. 6, for the localization of the focus of the 2010 Granada deep earthquake).

The geometry of the slab is more complicated than previously proposed in the literature (Bijwaard & Spakman 2000; Bezada *et al.* 2013). In our images, the high-velocity zone is not only attached to the surface east the internal Rif—as previously constrained by tomography (Bezada *et al.* 2013), geodesy (Pérouse *et al.* 2010) or seismicity (Buforn *et al.* 2004)—but also likely in some parts of the central Betics (Figs 8 and 9, see cross-sections EE′, II′, JJ′, OO′ and PP′), along the arc that connects the two fast anomalies observed at 135 km depth (Fig. 6). Those close to connected zones can account for the intermediate seismicity observed throughout the Alborán domain (e.g. Buforn *et al.* 2004; Mancilla *et al.* 2013b). At greater depths, *P*-wave anomalies end east from a line oriented NE/SW that connects the southeast Iberia to the internal Rif. In between the two lies the main part of the huge Alborán Sea fast anomaly, not connected with the surface. In comparison with other fast anomalies observed throughout the Mediterranean (e.g. Wortel & Spakman 2000; Piromallo & Morelli 2003), the Alborán high-velocity zone is relatively narrow and localizes on a small area at the surface, but the amount of material required to explain this anomaly—approximately 700 km long, 400 km wide and 150 km thick—represents a surprisingly big lithospheric remnant, regarding the present day extent of the Alborán domain. According to palaeo-geographic reconstructions of the western Mediterranean domain (e.g. Stampfli 2000; Stampfli *et al.* 2002; Rosenbaum *et al.* 2002b), the N-S width of oceanic lithosphere separating Iberia from Africa is only few hundred kilometres, while the length of the Ligurian palaeo-ocean is up to 700–800 km long in a approximately EW direction. Palaeogeographic reconstructions and our tomograms thus favour a subduction process coming from the E–NE or E–SE, progressively retreating to the W–SW or W–NW. Such a progression is in agreement with most models of evolution of the western Mediterranean (e.g. Lonergan & White 1997; Jolivet & Faccenna 2000; Gutscher *et al.* 2002; Rosenbaum *et al.* 2002a; Faccenna *et al.* 2004; Spakman & Wortel 2004; Bezada *et al.* 2013). The observed fast anomaly can also be derived from a more isolated subduction that would be restricted to the westernmost part of the Ligurian ocean (Vergés & Fernàndez 2012).

Differences between those models once again lie in the tectonic history of the Alborán domain. They generally propose the Alborán domain to be localized on the upper plate of a subduction starting from the Balearic margin (Lonergan & White 1997; Gutscher *et al.* 2002; Faccenna *et al.* 2004; Spakman & Wortel 2004). In this scenario, the Alborán domain has drifted from eastern Iberia and was accreted to the Iberian and African margins at its present day location by the roll-back of the Ligurian slab. This is not fully consistent with the absence of geological evidence for a Balearic origin of the Alborán domain (Platt *et al.* 2003) and requires a tricky arcuate westward slab roll-back to occur. Vergés & Fernàndez (2012) propose the Alborán domain to be localized on the subducting plate at close to its present day position, with a subduction initiation along the African margin. The Ligurian lithosphere is destroyed along an NE/SW subduction trench, followed by delamination of the lithospheric mantle of the Alborán domain and by slab break-off. This scenario is quite tempting, because geodynamically simpler than the one involving drift, it accounts well for the geometry of the anomaly we observe in our tomograms, but does not provide enough material to explain a 700 km long anomaly. Bezada *et al.* (2013), at last, propose a model in between these two and close to what is proposed for the Aegean domain by Tirel *et al.* (2013). In their model, the Alborán domain is located on the subducting plate, close to its present day location (to the east), with a subduction initiated along the Balearic margin, that continues under the Alborán crust delaminating its lithospheric mantle, and terminating west the Alborán domain beneath the Gibraltar strait. This model accounts for most geological and tectonic requirements. However, we do not agree with their proposition for a still active subduction in western Alborán. Our images clearly show that no connection exists beneath the Gibraltar strait, as anomalies appear only at approximately 100 to 150 km depth.

In our preferred model for the evolution of the Alborán Sea, the Ligurian slab, retreating from the Balearic margin, after consuming oceanized lithosphere east the Iberian coast, reaches the Alborán continental domain localized on the subducting plate and delaminates its lithospheric mantle. Asthenospheric temperatures at the base of the Alborán crust at that time caused the episode of

crustal anatexis around 20 Ma (Platt *et al.* 1998; Rossetti *et al.* 2010, 2013). As proposed by Bezada *et al.* (2013), subduction could have pursued west of the Alborán domain destroying a small oceanized lithosphere that separated the Alborán continental shred from the Iberian margin. Subduction of this piece of oceanic lithosphere and its westward to northwestward roll-back could then explain the calc-alkaline volcanism observed in the Alborán Sea (Duggen *et al.* 2004) and the westward displacement and extension of the Alborán domain (Platt *et al.* 1998). Our model, however, differs from Bezada *et al.* (2013) on what happens at the edges of the subduction. The fact that our images show that slab is attached to the surface at its edges, that is in the eastern internal Rif and central Betics, seems to indicate that, after the delamination of the Alborán lithospheric mantle, roll-back ended in these two zones. This subduction stopping is likely caused by the absence of an oceanic lithosphere to the south and the north of the Alborán domain that would have maintained the subduction process. These two domains anchor the southwestern and the northeastern boundaries of the slab, causing with the pursuing of the roll-back in its centre, the development of its arcuate geometry. With the termination of the subduction of the small oceanic lithosphere in western Alborán Sea, and NS convergence of Africa according to Iberia, slab break-off could have occurred beneath the Gibraltar Arc and the western Betics explaining the slow anomalies we observe close to the surface in this zones and the alkaline volcanism in Betics and northern Morocco (Duggen *et al.* 2005). Intermediate depth seismicity observed in the Rif and Betics ranges (e.g. Buforn *et al.* 2004; Mancilla *et al.* 2013b) can also indicate that delamination or tearing of the continental lithosphere in those regions is still active. Slab remnants localized between the two still attached edges, would have then sunk and likely folded, explaining the relatively large thickness of the anomaly (∼200 km) between 200 and 400 km depth.

4 CONCLUSION

We image the western Mediterranean upper mantle using multiple-frequency tomography from cross-correlation delay time measurements in six different frequency bands. This technique combined with dense seismic array and 4 yr of high-quality data allows us to provide new constraints on the evolution of these key zones for understanding the geodynamics of the Mediterranean basin.

We showed the presence, at lithospheric depths, of a relatively continuous low *P*-wave velocity zone extending from the southwestern Moroccan coast to the eastern Iberia crossing the Gibraltar strait. This anomaly is correlated at the surface with the Moroccan Atlas high topography and the Cenozoic volcanic fields, thus confirming the role of the dynamic topography during the High, Middle, and Anti-Atlas orogeny (Teixell *et al.* 2005). A lateral connection of the Moroccan Atlas anomaly with the Canary plume (e.g. Duggen *et al.* 2009) is, however, unlikely. The continuation of the anomaly to the north is probably caused by asthenospheric upwelling associated with slab break-off along the Gibraltar arc, and would have been spread around the Alborán basin by active mantle flow skirting the fast anomaly present in the upper mantle beneath the Alborán Sea (Alpert *et al.* 2013).

We confirm the slab-like nature of the 3-4 per cent anomaly imaged beneath the Alborán Sea, that extends down to the base of the transition zone. We show that its geometry is more complicated than previously proposed as it is connected with the surface only in two regions, beneath the eastern internal Rif on the African plate and

beneath the eastern internal Betics on the Iberian plate. We propose the slab to be the remnant of the Mesozoic Ligurian oceanic lithosphere and the Alborán lithospheric mantle, that faced a westward to northwestward roll-back since middle Oligocene. Subduction was halted along northern and southern edges of the Alborán continental domain causing tear and break-off of the slab localize in western Alborán. As a consequence, no active subduction exists directly beneath the Gibraltar arc.

REFERENCES

Alpert, L.A., Miller, M.S., Becker, T.W. & Allam, A.A., 2013. Structure beneath the Alboran from geodynamic flow models and seismic anisotropy, *J. geophys. Res. Solid Earth,* **118,** 1–13.

Babault, J., Teixell, A., Arboleya, M.-L. & Charroud, M., 2008. A late Cenozoic age for long-wavelength surface uplift of the Atlas Mountains of Morocco, *Terra Nova,* **20**(2), 102–107.

Bezada, M.J., Humphreys, E.D., Toomey, D.R., Harnafi, M., Dávila, J.M. & Gallart, J., 2013. Evidence for slab rollback in westernmost Mediterranean from improved upper mantle imaging, *Earth planet. Sci. Lett.,* **368,** 51–60.

Bijwaard, H. & Spakman, W., 2000. Non-linear global *P*-wave tomography by iterated linearized inversion, *Geophys. J. Int.,* **141**(1), 71–82.

Blanco, M.J. & Spakman, W., 1993. The P-wave velocity structure of the mantle below the Iberian Peninsula: evidence for subducted lithosphere below southern Spain, *Tectonophysics,* **221**(1), 13–34.

Bokelmann, G.H.R. & Maufroy, E., 2007. Mantle structure under Gibraltar constrained by dispersion of body waves, *Geophys. Res. Lett.,* **34**(22), L22305, doi:10.1029/2007GL030964.

Bolton, H. & Masters, G., 2001. Travel times of *P* and *S* from global digitial seismic networks: implications for the relative variation of *P* and *S* velocity in the mantle, *J. geophys. Res.,* **106**(B7), 12 527–13 540.

Buforn, E., Bezzeghoud, M., Udías, A. & Pro, C., 2004. Seismic sources on the Iberia-African plate boundary and their tectonic implications, *Pure appl. Geophys.,* **161**(3), 623–646.

Buforn, E., Pro, C., Cesca, S., Udías, A. & del Fresno, C., 2011. The 2010 Granada, Spain, deep earthquake, *Bull. seism. Soc. Am.,* **101**(5), 2418–2430.

Buontempo, L., Bokelmann, G.H.R., Barruol, G. & Morales, J., 2008. Seismic anisotropy beneath southern Iberia from SKS splitting, *Earth planet. Sci. Lett.,* **273**(3–4), 237–250.

Calvert, A. *et al.*2000. Geodynamic evolution of the lithosphere and upper mantle beneath the Alboran region of the western Mediterranean: constraints from travel time tomography, *J. geophys. Res.,* **105**(B5), 10 871–10 898.

Cuevas, J., Esteban, J.J. & Tubía, J.M., 2006. Tectonic implications of the granite dyke swarm in the Ronda peridotites (Betic Cordilleras, Southern Spain), *J. geol. Soc. Lond.,* **163**(4), 631–640.

Dahlen, F.A., Hung, S.-H. & Nolet, G., 2000. Fréchet kernels for finite-frequency traveltimes—I. theory, *Geophys. J. Int.,* **141**(1), 157–174.

Díaz, J. *et al.*, 2010. Mantle dynamics beneath the Gibraltar Arc (western Mediterranean) from shear-wave splitting measurements

on a dense seismic array, *Geophys. Res. Lett.,* **37**(18), L18304, doi:10.1029/2010GL044201.

Duggen, S., Hoernle, K.A., van den Bogaard, P. & Harris, C., 2004. Magmatic evolution of the Alboran region: the role of subduction in forming the western Mediterranean and causing the Messinian Salinity Crisis, *Earth planet. Sci. Lett.,* **218**(1–2), 91–208.

Duggen, S., Hoernle, K.A., van den Bogaard, P. & Garbe-Schönberg, D., 2005. Post-collisional transition from subduction to intraplate-type magmatism in the westernmost Mediterranean: evidence for continental-edge delamination of subcontinental lithosphere, *J. Petrol.,* **46**(6), 1155–1201.

Duggen, S., Hoernle, K.A., Hauff, F., Klügel, A., Bouabdellah, M. & Thirlwall, M.F., 2009. Flow of Canary mantle plume material through a subcontinental lithospheric corridor beneath Africa to the Mediterranean, *Geology,* **37**(3), 283–286.

Faccenna, C., Piromallo, C., Crespo-Blanc, A., Jolivet, L. & Rossetti, F., 2004. Lateral slab deformation and the origin of the western Mediterranean arcs, *Tectonics,* **23**(1), TC1012, doi:10.1029/2002TC001488.

Frizon de Lamotte, D., Saint Bezar, B. & Bracène, R., 2000. The two main steps of the Atlas building and geodynamics of the western Mediterranean, *Tectonics,* **19**(4), 740–761.

Frizon de Lamotte, D., Leturmy, P., Missenard, Y., Khomsi, S., Ruiz, G., Saddiqi, O., Guillocheau, F. & Michard, A., 2009. Mesozoic and Cenozoic vertical movements in the Atlas system (Algeria, Morocco, Tunisia): an overview, *Tectonophysics,* **475**(1), 9–28.

Frizon de Lamotte, D., Raulin, C., Mouchot, N., Wrobel-Daveau, J.-C., Blanpied, C. & Ringenbach, J.-C., 2011. The southernmost margin of the Tethys realm during the Mesozoic and Cenozoic: initial geometry and timing of the inversion processes, *Tectonics,* **30**(3), TC3002, doi:10.1029/2010TC002691.

Fullea, J., Fernàndez, M., Afonso, J.C., Vergés, J. & Zeyen, H., 2010. The structure and evolution of the lithosphere-asthenosphere boundary beneath the Atlantic-Mediterranean Transition Region, *Lithos,* **120**(1–2), 74–95.

Goes, S., Spakman, W. & Bijwaard, H., 1999. A lower mantle source for central european volcanism, *Science,* **286**(5446), 1928–1931.

Gomez, F., Allmendinger, R., Barazangi, M., Er-Raji, M. & Dahmani, M., 1998. Crustal shortening and vertical strain partitioning in the Middle Atlas Mountains of Morocco, *Tectonics,* **17**(4), 520–533.

Gutscher, M.-A., Malod, J., Rehault, J.-P., Contrucci, I., Klingelhoefer, F., Mendes-Victor, L. & Spakman, W., 2002. Evidence for active subduction beneath Gibraltar, *Geology,* **30**(12), 1071–1074.

Gutscher, M.-A. *et al.* 2012. The gibraltar subduction: a decade of new geophysical data, *Tectonophysics,* **574–575,** 72–91.

Hoernle, K.A., Zhang, Y.-S. & Graham, D., 1995. Seismic and geochemical evidence for large-scale mantle upwelling beneath the eastern Atlantic and western and central Europe, *Nature,* **374**(6517), 34–39.

Houser, C., Masters, G., Shearer, P.M. & Laske, G., 2007. Shear and compressional velocity models of the mantle from cluster analysis of long-period waveforms, *Geophys. J. Int.,* **174**(1), 195–212.

Jolivet, L. & Faccenna, C., 2000. Mediterranean extension and the Africa-Eurasia collision, *Tectonics,* **19**(6), 1095–1106.

Jolivet, L., Augier, R., Robin, C., Suc, J.-P. & Rouchy, J.M., 2006. Lithospheric-scale geodynamic context of the Messinian salinity crisis, *Sediment. Geol.,* **188–189,** 9–33.

Kennett, B.L.N. & Engdahl, E.R., 1991. Traveltimes for global earthquake location and phase identification, *Geophys. J. Int.,* **105**(2), 429–465.

King, S.D. & Ritsema, J., 2000. African hot spot volcanism: small-scale convection in the upper mantle beneath cratons, *Science,* **290**(5494), 1137–1140.

Lonergan, L. & White, N., 1997. Origin of the Betic-Rif mountain belt, *Tectonics,* **16**(3), 504–522.

Lou, X. & van der Lee, S., 2014. Observed and predicted North American teleseismic delay times, *Earth planet. Sci. Lett.,* doi:10.1016/j.epsl.2013.11.056.

Lou, X., van der Lee, S. & Lloyd, S., 2013. AIMBAT: a Python/Matplotlib tool for measuring teleseism arrival times, *Seismol. Res. Lett.,* **84**(1), 85–93.

Lustrino, M. & Wilson, M., 2007. The circum-mediterranean anorogenic Cenozoic igneous province, *Earth-Sci. Rev.,* **81**(1–2), 1–65.

Mancilla, F. *et al.* 2012. Crustal thickness variations in northern Morocco, *J. geophys. Res.,* **117**(B2), B02312, doi:10.1029/2011JB008608.

Mancilla, F. & Díaz, J. TopoIberia Scientific Team, 2013a. High resolution Moho topography map beneath Iberia and Northern Morocco from RF analysis, *Geophys. Res. Abstract,* **15**, EGU2013–7628.

Mancilla, F., Stich, D., Martín, R., Morales, J., Fernandez-Ros, A., Páez, R. & Pérez-Peña, A., 2013b. Delamination in the Betic range: deep structure, seismicity, and GPS motion, *Geology,* **41**(3), 307–310.

Mercerat, E.D. & Nolet, G., 2013. On the linearity of cross-correlation delay times in finite-frequency tomography, *Geophys. J. Int.,* **192**(2), 681–687.

Mezcua, J. & Rueda, J., 1997. Seismological evidence for a delamination process in the lithosphere under Alboran Sea, *Geophys. J. Int.,* **129**(1), F1–F8.

Miller, M.S., Allam, A.A., Becker, T.W., Di Leo, J.F. & Wookey, J., 2013. Constraints on the tectonic evolution of the westernmost Mediterranean and northwestern Africa from shear wave splitting analysis, *Earth planet. Sci. Lett.,* **375**, 234–243.

Missenard, Y. & Cadoux, A., 2012. Can Moroccan Atlas lithospheric thinning and volcanism be induced by Edge-Driven Convection, *Terra Nova,* **24**(1), 27–33.

Missenard, Y., Zeyen, H., Frizon de Lamotte, D., Leturmy, P., Petit, C., Sébrier, M. & Saddiqi, O., 2006. Crustal versus asthenospheric origin of relief of the Atlas Mountains of Morocco, *J. geophys. Res.,* **111**(B3), B03401, doi:10.1029/2005JB003708.

Montelli, R., Nolet, G., Dahlen, F.A., Masters, G., Engdahl, E.R. & Hung, S.-H., 2004. Finite-frequency tomography reveals a variety of plumes in the mantle, *Science,* **303**(5656), 338–343.

Montelli, R., Nolet, G., Dahlen, F.A. & Masters, G., 2006. A catalogue of deep mantle plumes: new results from finite-frequency tomography, *Geochem. Geophys. Geosyst.,* **7**(11), Q11007, doi:10.1029/2006GC001248.

Morales, J., Serrano, I., Jabaloy, A., Galindo-Zaldívar, J., Zhao, D., Torcal, F., Vidal, F. & González-Lodeiro, F., 1999. Active continental subduction beneath the Betic Cordiellera and the Alborán Sea, *Geology,* **27**(8), 735–738.

Nolet, G., 2008. *A Breviary for Seismic Tomography,* Cambridge Univ. Press.

Obayashi, M., Suetsugu, D. & Fukao, Y., 2004. PP-P differential travel time measurement with crustal correction, *Geophys. J. Int.,* **157**(3), 1152–1162.

Paige, C.C. & Saunders, M.A., 1982. LSQR: an algorithm for sparse, linear equations and sparse least square, *Trans. Math. Software,* **8**(1), 43–71.

Pavlis, G.L. & Vernon, F.L., 2010. Array processing of teleseismic body waves with the USArray, *Comput. Geosci.,* **36**(7), 910–920.

Pérouse, E., Vernant, P., Chéry, J., Reilinger, R. & McClusky, S., 2010. Active surface deformation and sub-lithospheric processes in the western Mediterranean constrained by numerical models, *Geology,* **38**(9), 823–826.

Piromallo, C. & Morelli, A., 2003. *P* wave tomography of the mantle under the Alpine-Mediterranean area, *J. geophys. Res.,* **108**(B2), 2065, doi:10.1029/2002JB001757.

Piromallo, C., Gasperini, D., Macera, P. & Faccenna, C., 2008. A late Cretaceous contamination episode of the European-Mediterranean mantle, *Earth planet. Sci. Lett.,* **268**(1–2), 15–27.

Platt, J.P. & Houseman, G., 2003. Evidence for active subduction beneath Gibraltar: comment and reply: COMMENT, *Geology,* **31**(1), doi:10.1130/0091-7613-31.1.e22.

Platt, J.P. & Vissers, R.L.M., 1989. Extensional collapse of thickened continental lithosphere: a working hypothesis for the Alboran Sea and Gibraltar arc, *Geology,* **17**(6), 540–543.

Platt, J.P. & Whitehouse, M.J., 1999. Early Miocene high-temperature metamorphism and rapide exhumation in the Betic Cordillera (Spain): evidence from U-Pb zircon ages, *Earth planet. Sci. Lett.,* **171**(4), 591–605.

Platt, J.P., Soto, J.-I., Whitehouse, M.J., Hurford, A.J. & Kelley, S.P., 1998. Thermal evolution, rate of exhumation, and tectonic significance of metamorphic rocks from the floor of the Alboran extensional basin, western Mediterranean, *Tectonics,* **17**(5), 671–689.

Platt, J.P., Allerton, S., Kirler, A., Mandeville, C., Mayfield, A., Platzman, E.S. & Rimi, A., 2003. The ultimate arc: differential displacement, oroclinal bending, and vertical axis rotation in the External Betic-Rif arc, *Tectonics,* **22**(3), 1017, doi:10.1029/2001TC001321.

Ramdani, F., 1998. Geodynamic implications of intermediate-depth earthquakes and volcanism in the intraplate Atlas mountains (Morocco), *Phys. Earth planet. Inter.,* **108**(3), 245–260.

Ritsema, J., van Heijst, H.J., Woodhouse, J.H. & Deuss, A., 2009. Long-period body wave traveltimes through the crust: implication for crustal corrections and seismic tomography, *Geophys. J. Int.,* **179**(2), 1255–1261.

Rosenbaum, G., Lister, G.S. & Duboz, C., 2002a. Reconstruction of the tectonic evolution of the western Mediterranean since the Oligocene, *J. Virtual Explor.,* **8,** 107–130.

Rosenbaum, G., Lister, G.S. & Duboz, C., 2002b. Relative motions of Africa, Iberia and Europe during Alpine orogeny, *Tectonophysics,* **359**(1–2), 671–689.

Rossetti, F., Theye, T., Lucci, F., Bouybaouene, M.L., Dini, A., Gerdes, A., Phillips, D. & Cozzupoli, D., 2010. Timing and modes of granite magmatism in the core of the Alboran Domain, Rif chain, northern Morocco: implicatiobs for the Alpine evolution of the western Mediterranean, *Tectonics,* **29**(2), TC2017, doi:10.1029/2009TC002487.

Rossetti, F., Dini, A., Lucci, F., Bouybaouene, M.L. & Faccenna, C., 2013. Early Miocene strike-slip tectonics and granite emplacement in the Alboran Domain (Rif Chain, Morocco): significance for the geodynamic evolution of Western Mediterranean, *Tectonophysics,* **608**, 774–791.

Seber, D., Barazangi, M., Ibenbrahim, A. & Demnati, A., 1996a. Geophysical evidence for lithospheric delamination beneath the Alboran Sea and Rif-Betic mountains, *Nature,* **379**(6568), 785–790.

Seber, D., Barazangi, M., Tadili, B.A., Ramdani, M., Ibenbrahim, A. & Ben Sari, D., 1996b. Three-dimensional upper mantle structure beneath the intraplate Atlas and interplate Rif mountains of morocco, *J. geophys. Res.,* **101**(B2), 3125–3138.

Sigloch, K. & Nolet, G., 2006. Measuring finite-frequency body-wave amplitudes and traveltimes, *Geophys. J. Int.,* **167**(1), 271–287.

Sigloch, K., McQuarrie, N. & Nolet, G., 2008. Two-stage subduction history under North America inferred from multiple-frequency tomography, *Nat. Geosci.,* **1**(7), 458–462.

Spakman, W. & Wortel, M.J.R., 2004. Tomographic view on western mediterranean geodynamics, *The TRANSMED Atlas. The Mediterranean Region from Crust to Mantle,* pp. 31–52, Springer-Verlag, doi:10.1007/978-3-642-18919-7_2.

Spakman, W., van der Lee, S. & van der Hilst, R., 1993. Travel-time tomography of the European-Mediterranean mantle down to 1400 km, *Phys. Earth planet. Inter.,* **79**(1–2), 3–74.

Stampfli, G.M., 2000. Tethyan oceans, *Geol. Soc., Lond., Special Pub.,* **173,** 1–23.

Stampfli, G.M., Borel, G.D., Marchant, R. & Mosar, J., 2002. Western Alps geological constraints on western Tethyan reconstructions, *J. Virtual Explor.,* **8,** 77–106.

Teixell, A., Arboleya, M.-L., Julivert, M. & Charroud, M., 2003. Tectonic shortening and topography in central High Atlas (Morocco), *Tectonics,* **22**(5), 1051, doi:10.1029/2002TC001460.

Teixell, A., Ayarza, P., Zeyen, H., Fernàndez, M. & Arboleya, M.-L., 2005. Effects of mantle upwelling in a compressional setting: the Atlas Mountains of Morocco, *Terra Nova,* **17**(5), 456–461.

Tian, Y., Hung, S.-H., Nolet, G., Montelli, R. & Dahlen, F.A., 2007a. Dynamic ray tracing and traveltime corrections for global seismic tomography, *J. Comput. Phys.,* **226**(1), 672–687.

Tian, Y., Montelli, R., Nolet, G. & Dahlen, F.A., 2007b. Computing traveltime and aplitude sensitivity kernels in finite-frequency tomography, *J. Comput. Phys.,* **226**(2), 2271–2288.

Tirel, C., Brun, J.-P., Burov, E.B., Wortel, M.J.R. & Lebedev, S., 2013. A plate tectonics oddity: caterpillar-walk exhumation of subducted continental crust, *Geology,* **41**(5), 555–558.

VanDecar, J.C. & Crosson, R.S., 1990. Determination of teleseismic relative phase arrival times using multi-channel cross-correlation and least squares, *Bull. seism. Soc. Am.,* **80**(1), 150–169.

Vergés, J. & Fernàndez, M., 2012. Tethys-Atlantic interaction along the Iberia-Afraice plate boundary: the Betic-Rif orogenic system, *Tectonophysics,* **579,** 144–172.

Wessel, P. & Smith, W.H.F., 1998. New, improved version of generic mapping tools released, *EOS, Trans. Am. geophys. Un.,* **79**(47), 579.

Wessel, P., Smith, W.H.F., Scharroo, R., Luis, J. & Wobbe, F., 2013. Generic mapping tools: improved version released, *EOS, Trans. Am. geophys. Un.,* **94**(45), 409–410.

Wortel, M.J.R. & Spakman, W., 2000. Subduction and slab detachment in the mediterranean-carpathian region, *Science,* **290**(5498), 1910–1917.

Zeck, H.P., 1996. Betic-rif orogeny: subduction of Mesozoic Tethys lithosphere under eastward drifting Iberia, slab detachment shortly before 22 Ma, and subsequent uplift and extensional tectonics, *Tectonophysics,* **254**(1–2), 1–16.

Zeyen, H., Ayarza, P., Fernàndez, M. & Rimi, A., 2005. Lithospheric structure under the western African-European plate boundary: a transect across the Atlas Mountains and the Gulf of Cadiz, *Tectonics,* **24**(2), TC2001, doi:10.1029/2004TC001639.

APPENDIX A:

VanDecar & Crosson (1990) use the differences in arrival time between each pair of seismograms $u_i(t)$, $u_j(t)$ in a network of N stations. Thus, we measure:

$$\Delta T_{ij} = T_i - T_j \quad (i < j = 1, ..., N). \tag{A1}$$

Since $T_{ij} = -T_{ji}$ we only need to cross-correlate for $j > i$. Though in principle one could use all ΔT_{ij} directly in a tomographic inversion this poses obvious problems of inefficiency of use of memory and CPU. It would be much better to invert the absolute values T_i rather than the differences. However, even though (A1) gives us $N(N - 1)/2$ equations with N unknowns, individual arrival times cannot be determined from it because any constant added to all arrival times would subtract out. In other words, if the set of absolute times $\{T_i\}$ satisfies (A1), the set $\{T_i + c\}$ does this also. The term absolute is therefore not quite correct, and we shall use the term quasi-absolute in what follows.

Once we recognize that there is always a freely floating constant, we may impose this constant to be such that *on average* the arrivals satisfy the predicted average for the background model:

$$\frac{1}{N} \sum_{i=1}^{N} T_i = \frac{1}{N} \sum_{i=1}^{N} T_i^{\text{pred}}. \tag{A2}$$

Usually, (A2) is not a true constraint on the Earth's velocity, since in the tomographic inversions one commonly allows for a correction of the earthquake's origin time T_0. Since T_0 is, again, the same for every estimate T_i, this allows for a correction in the average, if needed, and avoids a strong bias imposed by the background model. In this study, we use a variant on this constraint, that adds also some robustness to the solution of the system of equations and guards against cycle skips and other outliers. We add not one, but N equations with a small weight ϵ, of the form:

$$\epsilon T_i = \epsilon T_i^{\text{pred}} \quad (i = 1, ...N). \tag{A3}$$

Estimating delays by picking the maximum of the cross-correlation signal does not work very well if the waveforms are very different and give rise to cycle skips. In general, one shall therefore wish to avoid to use delays with associated correlation coefficients that are small. Mercerat & Nolet (2013) find that imposing a minimum correlation coefficient of 0.8 avoids cycle skips at the highest bandpass frequencies in a cross-borehole simulation. Eliminating certain station pairs from (A1) does not necessarily lead to

an underdetermined system: all stations pairs for a particular station would have to be removed to make this station delay unconstrained except for the condition (A3). In this study, we imposed a lower limit of 0.85 on the broad-band correlations, and reject a seismogram if none of its pair-wise correlations reaches this limit. This also turns out to be an efficient way to winnow high noise seismograms out of the data set.

We therefore adapt the VanDecar-Crosson equation by imposing a minimum correlation coefficient $R_{\lim}$ and combine it with the regularization eq. (A3):

$$\Delta T_{ij} = T_i - T_j \quad (i < j = 1, ..., N) \quad R > R_{\lim}.$$
$$\epsilon T_i = \epsilon T_i^0 \quad (i = 1, ...N). \tag{A4}$$

This choice of regularization was easier to handle by our software that takes the full traveltime, rather than delays, as input so as to be able to test different background models. Its function is however the same as the strategy followed by VanDecar & Crosson (1990). Thus, instead of following VanDecar & Crosson (1990) who set the sum $\sum_i T_i$ to 0, we damp each delay slightly towards the time T_i^0 predicted for the background model; by choosing $\epsilon \ll N$ these additional equations do not influence the result much. In tests we found that even $\epsilon = 1$ works, but generally we use $\epsilon = 0.1$.

The system (A4) is a system of $K \leq N(N + 1)/2$ equations (if we include the N damping rows) with N unknowns. The system is sparse (only two non-zeroes in each row) which we solve using the sparse matrix solver LSQR (Paige & Saunders 1982). Though theoretically it makes no difference in the final result, we found that LSQR converges much faster if we formulate the inverse problem in terms of delays $\delta T_i = T_i - T_i^0$ instead of quasi-absolute times T_i. The modified VanDecar-Crosson equations are therefore rewritten:

$$(T_i - T_i^0) - (T_j - T_j^0) = \Delta T_{ij} - (T_i^0 - T_j^0),$$
$$(i < j = 1, ..., N), \quad R > R_{\lim}.$$
$$\epsilon(T_i - T_i^0) = 0 \quad (i, j = 1, ..., N). \tag{A5}$$

In symbolic notation, we write this system as:

$$\begin{pmatrix} A \\ \epsilon I \end{pmatrix} \delta T = \begin{pmatrix} b \\ 0 \end{pmatrix}. \tag{A6}$$

The fit that is obtained to the eqs (A4) or (A5) gives valuable information on the measurement errors, assuming that the delays fit (A4) exactly if it were not for measurement errors. If we have K pair-wise cross-correlations for station i, we can—following VanDecar & Crosson (1990)—estimate the measurement error by computing the average squared residual: $res_{ij} = \Delta T_{ij} - (T_i - T_j)$ for observed ΔT_{ij} and solved T_i's. The rms timing uncertainty is then given by a standard error:

$$\sigma_i = \left(\frac{1}{K - 2} \sum_j res_{ij}^2 \right)^{\frac{1}{2}}, \tag{A7}$$

where the sum is over all K observed cross-correlation pairs (i, j). The assumption that the delays fit (A4) exactly is evident for onset times that satisfy ray theory. In the case of cross-correlation times the validity of the assumption is less obvious. For example, ΔT_{13} is measured independently from ΔT_{12} and ΔT_{23}, and therefore not guaranteed to be equal to their sum.

However, in finite-frequency theory one assumes a linear relationship of the form:

$$\delta T_i = \int K_i(\boldsymbol{r}) \, \delta \ln V_P(\boldsymbol{r}) \, \mathrm{d}^3 \boldsymbol{r}. \tag{A8}$$

Mercerat & Nolet (2013) show that this linearized relationship is valid for mantle-type heterogeneities, in which case we find again that $\delta \Delta T_{ij} = \delta T_i - \delta T_j$. Any deviations from this linearity will show up as added residuals. If we lump such theory errors together with measurement errors, (A7) then still gives an estimate of the errors in our resulting δT_i. To account for systematic errors due to unknown bias, we generally add a small extra error of 0.2 s to the standard error estimated by (A7).

Our method for cross-correlating signals differs from that of Pavlis & Vernon (2010), who correlate with a reference signals selected from the seismograms. Lou *et al.* (2013) and Lou & van der Lee (2014) apply the VanDecar-Crosson equations like we do, but determine the constant time offset by eye rather than by comparison with a background model. In addition, we use band-pass filtering to extract body wave dispersion.

APPENDIX B:

The cross-correlation between two signals $s_i(t)$ and $s_j(t)$ is defined as the time of the maximum in the cross-correlogram $\gamma_{ij}(t)$:

$$\gamma_{ij}(t) = \frac{1}{E} \int_{t_i}^{t_j} s_i(\tau) s_j(\tau - t) \, \mathrm{d}\tau, \tag{B1}$$

where $E = \int [s_i(\tau)^2 s_j(\tau)^2]^{\frac{1}{2}} \mathrm{d}\tau \approx \int s_i(\tau)^2 \mathrm{d}\tau$ is a normalizing factor.

The optimal time windowing before cross-correlation is a subject that has not yet been explored in detail in the literature of finite-frequency tomography. We follow Mercerat & Nolet (2013) and define the window boundaries t_1 and t_2 as:

$$t_1 = t_i^{\text{pred}} - \sigma - d_{\text{taper}}, \tag{B2}$$

$$t_2 = t_i^{\text{pred}} + \sigma + f_c^{-1} + d_{\text{pulse}} + d_{\text{taper}}, \tag{B3}$$

where t_i^{pred} is the predicted arrival time in station i with uncertainty σ, d_{pulse} is the duration of the body wave pulse on the broad-band record, f_c is the central frequency of the passband filter and d_{taper} is the duration of the windowing taper. For most earthquakes except the very largest ones, the duration of a P or S wave is limited in time, and smaller than that of the longer periods of interest. In the case of the real Earth, some energy does arrive later because of scattering from a volume around the shortest time path. Clearly, the length of the time window we choose determines how much of this energy is going to be included in the cross-correlogram. Though finite-frequency kernels take such energy into account, we cannot choose a very large window without running the risk to include other phases (such as PP, or pP phases for a deep event) that requires them to be summed in the expressions for the Fréchet kernel. It greatly simplifies the theory—and probably also the stability of the inversion—if one sticks to a short window with arrivals close to the direct ray. If we include up to the second Fresnel zone, this means we choose a window with a length that is about twice the longest period considered. This implies choosing different window lengths for different periods. This is the reason (B3) contains the inverse of the bandpass frequency f_c^{-1}.

SUPPORTING INFORMATION

Additional Supporting Information may be found in the online version of this article:

The Supporting Information is composed by three figures presenting vertical cross-sections through the two checkerboard test models, for the section lines used in Figs 7–9.

Figure S1: (a) Vertical cross-sections through the 300 km checkerboard test for section lines used in Fig. 7. (b) Vertical cross-sections through the 150-km checkerboard test for section lines used in Fig. 7. Thick dotted black lines show limits of the transition zone.
Figure S2: (a) Vertical cross-sections through the 300-km checkerboard test for section lines used in Fig. 8. (b) Vertical cross-sections through the 150-km checkerboard test for section lines used in Fig. 8. Thick dotted black lines show limits of the transition zone.
Figure S3: (a) Vertical cross-sections through the 300-km checkerboard test for section lines used in Fig. 9. (b) Vertical cross-sections through the 150-km checkerboard test for section lines used in Fig. 9. Thick dotted black lines show limits of the transition zone.
Figure S4: Left: horizontal cross-section at 70 km depth through a −4 per cent gaussian anomalies input model that mimic geometry of the slow *P*-wave anomalies in the top 200 km of the topographic model (Fig. 6). Right: Output model.
Figure S5: Left: horizontal cross-section at 70 km depth through a −4 per cent gaussian anomalies input model that mimic geometry of the slow *P*-wave anomalies in the top 200 km of the topographic model (Fig. 6). Anomalies are further one from the others compared with Fig. S4. Right: Output model.
Figure S6: (a) Vertical cross-sections through the input model presented on Fig. S4 for section lines used in Fig. 8. Dotted black lines show limits of the transition zone. (b) Vertical cross-sections through the output model presented on Fig. S4 right for section lines used in Fig. 8.
Figure S7: (a) Vertical cross-sections through the input model presented on Fig. S5 for section lines used in Fig. 8. Dotted black lines show limits of the transition zone. (b) Vertical cross-sections through the output model presented on Fig. S5 right for section lines used in Fig. 8 (http://mnras.oxfordjournals.org/lookup/suppl/doi:10.1093/gji/ggu214/-/DC1).

Please note: Oxford University Press is not responsible for the content or functionality of any supporting materials supplied by the authors. Any queries (other than missing material) should be directed to the corresponding author for the article.